Displacement and Strain Measurement with Automated Grid Methods

by J.S. Sirkis and T.J. Lim

ABSTRACT—An image-processing-based automated grid method is investigated to determine the method's displacement and strain accuracy limits, and how these limits are influenced by the choice of camera-calibration models. A CCD camera and a PC-based frame grabber are used to record grid spot motion, then ordering and centroiding are used to identify each spot and calculate their individual displacements. The displacements are fitted with a moving biquadratic surface, and the strains are obtained by analytical differentiation of that surface. Camera-calibration models which are considered include various combinations of image-perspective transformation, image stretching, and elliptical-lens distortion. The strain and displacement accuracy are explored through rigid-body motion and uniaxial tension tests. In the process, sensitivity to in-plane and out-of-plane rigid-body translation, and extreme sensitivity to in-plane rigid-body rotation (for non-synchronized frame grabbers) are confirmed. It is found that under the best conditions the displacement accuracy is .015 pixels and that the strain accuracy is 120 microstrain. Finally, the automated grid method is used to investigate the strains developed in an aluminum perforated strip subjected to uniaxial tension.

Introduction

Grid methods can be automated by taking advantage of solid-state video technology and pattern-recognition algorithms. The potential advantages of automated grid methods over conventional grid methods are increased speed and accuracy. The primary advantage grid methods enjoy over the techniques which are traditionally recognized as more accurate is that specialized training is not needed to interpret the grid-method results, and that no additional effort is required for simultaneous measurement of both the horizontal and vertical displacement fields. The grid method discussed here consists of automatic tracking of round black grid spots placed on a white specimen.[1] Prior knowledge that the grid will have these simple characteristics (round and black) enables one to use relatively uncomplicated image-processing and pattern-recognition techniques to extract the grid-spot motion. Diffraction-based grid methods[2-5] can also be interrogated using solid-state video technology and hence

they also can be considered as automated grid methods. These methods use the discrete or optical Fourier power spectrum to infer strain at a point, and some form of external scanning device to find the full strain fields. The term automated grid method will be restricted in this paper to refer to only those methods using solid-state video technology for direct measurement of relative motion of grid spots or lines. This latter automated grid method is easy to implement; as a result, full-field strain analysis can be accomplished in roughly 120 seconds of personal computer CPU time.

Charge-coupled-device (CCD) technology was first used to track high contrast spots in 1980 for pointing applications in space-born telescopes.[6] Sevenhuijsen[1] first adapted this idea for solid-mechanics applications in 1984. Fail and Taylor[7] followed by developing a general pattern recognition algorithm for plane motion analysis. Then Sirkis and Taylor[8] adapted this concept to provide boundary conditions for a structural-analysis computer code. A detailed theoretical analysis of the grid-tracking algorithm presented by Sirkis[9] showed that spot geometric characteristics and grey-level profile play an important role in the accuracy and sensitivity of this type of automated grid method.[9] Further, Chao et al.[10] found that camera calibration can affect the strain accuracy of stereo digital correlation methods by as much as 30 percent. The present paper explores automated grid methods as a tool for measuring both displacement and strain. The emphasis is on establishing the experimental limits on the displacement and strain accuracy of this class of automated grid methods, and to discern the influence which the camera calibration model choice has on these accuracy limits. As an example of the implementation of such an automated grid method, the strain field developed in an aluminum perforated strip subjected to a uniaxial strain field is investigated.

Automated Grid Method

The automated grid method discussed here consists of tracking the individual displacements of each grid spot in an array of high contrast round spots. A CCD video camera and a personal-computer-based image-processing system are used to digitize the spot locations after each deformation increment. The spots are located with a histogram-based grey-level thresholding and their precise positions are found using a centroid algorithm.[9] Each spot is uniquely identified in each of the sequence of

J.S. Sirkis (SEM Member) is Assistant Professor, and T.J. Lim is Undergraduate Student, Department of Mechanical Engineering, University of Maryland, College Park, MD 20742.

images by the spot's position relative to its neighbors.[7] Icons are not required since rigid-body rotation is experimentally kept small enough that each spot is uniquely identifiable.[7] The array of high contrast spots is replicated on to the specimen by using the 'picture-layer'[11] procedure as described in Ref. 12.

Calibration

A grid, or any scene for that matter, experiences a series of transformations before it is finally stored in the computer's memory as a digital image. The most common types of transformations include coordinate translation and rotation, lens distortion, perspective transformation, and CCD image stretching.[13] Each transformation introduces errors in the actual centroid calculations, which in turn reduces the accuracy of subsequent strain calculations. A general pinhole camera calibration which includes all of the above transformations will be developed, and the relevance of each transformation assessed.

The following camera calibration which accounts for camera coordinate-system rotation, variable magnification, and second-order elliptical lens distortion[10,13] is predicated on the pinhole camera assumption. Although the pinhole camera assumption presents obvious limitations in modeling the multilens systems commonly used with video cameras, the mathematical convenience provided by the pinhole model warrants its use. This approach to camera calibration is certainly not new[9,10,13] so only rough coverage is provided here.

The camera is positioned relative to a fixed-world coordinate system (X_w, Y_w, Z_w), where the subscript w refers to 'world.' If one assumes for the moment that the camera acts as a pinhole, then a point in the undistorted camera-image plane (X_u, Y_u, Z_u), where the subscript u refers to 'undistorted,' maps to a point in the world coordinate system by[10,12]

$$X_w = \frac{f}{Z_w - f} (r_1 X_u + r_2 Y_u + t_1) \tag{1a}$$

$$Y_w = \frac{f}{Z_w - f} (r_3 X_u + r_4 Y_u + t_2) \tag{1b}$$

where f is the focal length of the pinhole camera, r_i ($i = 1, \ldots, 4$) and t_i ($i = 1, 2$) are respectively rigid-body rotations and translations between the world and undistorted camera-coordinate systems. Elliptical-lens distortion can be included into the model by extending the equations used by Tsai.[13]

$$X_u = (1 + k_1 R_d^2 + k_2 R_d^4) X_d \tag{2a}$$

and

$$Y_u = (1 + k_3 R_d^2 + k_4 R_d^4) Y_d \tag{2b}$$

The (X_d, Y_d) in the above equation are the distorted coordinates in the camera-image plane. $R_d^2 = X_d^2 + Y_d^2$, $k_i (i = 1, \ldots, 4)$ are the lens-distortion parameters. The subscript d refers to 'distorted'.

Finally, the distorted camera coordinates are mapped to the frame-grabber coordinate system (X_f, Y_f), where the subscript f refers to the 'frame grabber.' The transformation to the frame-grabber coordinates is known as 'image stretching' and only occurs in hardware where the camera and frame grabber are not synchronized. Since this is a normal characteristic in most digital-image-processing equipment, image stretching is included in the camera model. Unlike lens distortion and perspective transformations, image stretching is caused by the electronic hardware; more specifically, the image stretching is caused by resampling of the CCD image rows by the frame grabber. Each row of image data is sampled by the CCD camera at a fixed frequency, F_c, creating a fixed number of data points per row, N_c. The image signal is then converted to analog for a row by row transmission to the frame grabber. That is, one row in the CCD camera is mapped to one row in the frame grabber. The frame grabber resamples the analog row signals at a frequency, F_f, which is different from F_c. Therefore, the number of data points in the frame grabber memory is $N_f = (F_f/F_c)N_c$. The resampling effectively stretches the row data. A Sony XC-38 CCD camera ($F_c = 7.159$ MHz) and a Matrox PIP-1024B frame grabber ($F_f = 10.33$ MHz) are used in the tests reported in this paper.

The distorted camera coordinates (X_d, Y_d) are mapped to the frame-grabber coordinate system (X_f, Y_f) by

$$X_f = \left(\frac{F_f}{F_c}\right) \frac{X_d}{d_x} \tag{3a}$$

and

$$Y_f = \frac{Y_d}{d_y} \tag{3b}$$

where (F_f/F_c) is the stretching due to resampling, and d_x and d_y are the horizontal and vertical pixel dimensions (provided by the manufacturer). Equations (1), (2) and (3) are combined to form a mapping from world coordinates to the distorted coordinate system stored in the computer memory. This mapping takes the form of

$$X_w = a_1 X_f + a_2 Y_f + a_3 + a_4 X_f R_d^2 + a_5 Y_f R_d^2 + a_6 X_f R_d^4$$
$$+ a_7 Y_f R_d^4 \tag{4a}$$

and

$$Y_w = a_8 X_f + a_9 Y_f + a_{10} + a_{11} X_f R_d^2 + a_{12} Y_f R_d^2 + a_{13} X_f R_d^4$$
$$+ a_{14} Y_f R_d^4 \tag{4b}$$

where a_i ($i = 1, 2, \ldots, 14$) are the unknown aggregate mapping coefficients, and R_d is related to the frame coordinates by

$$R_d^2 = d_x^2 \left(\frac{F_c}{F_f}\right)^2 X_f^2 + d_y^2 Y_f^2 \tag{5}$$

The aggregate mapping coefficients (a_i) do not have physical meaning; each are combinations of coordinate-system translations and rotations, the lens focal length, the four-lens distortion coefficients, and the x- and y-magnification factors as described in Ref. 12. A linear-calibration procedure is made possible by forming these 'aggregate' coefficients[14]; otherwise nonlinear programming methods are required.[10,13] The mapping coefficients are determined by first capturing an image of a square array of control points (grid spots) which have known positions in the world coordinate system. The frame-grabber coordinates of the control points are then calculated with the centroid algorithm. Equations (4) and (5) are used to formulate a least-squares system for the linear coefficients, a_i. This least-squares system matrix is solved with singular-value decomposition.

Strain Calculations

A least-squares numerical-differentiation scheme is used to calculate the displacement gradients. The local displacement field is fit with a moving biquadratic surface then differentiated using analytical methods. The function to which the local displacement field is fit takes the form of[15]

$$u - u_o = b_1 + b_2 X_w + b_3 Y_w + b_4 X_w Y_w + b_5 Y_w^2 + b_6 X_w^2$$

(6a)

and

$$v - v_o = b_7 + b_8 X_w + b_9 Y_w + b_{10} X_w Y_w + b_{11} Y_w^2 + b_{12} X_w^2$$

(6b)

In eq (6), (u, v) are the displacements at the current load, (u_o, v_o) are the displacements in a reference state, and b_i $(i = 1, 2, \ldots, 12)$ are the fitting constants found using least squares.[7]
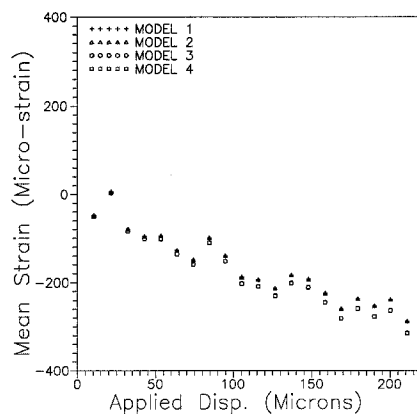

Fig. 1—X-strain error induced by in-plane rigid-body translation with the four-camera calibration models
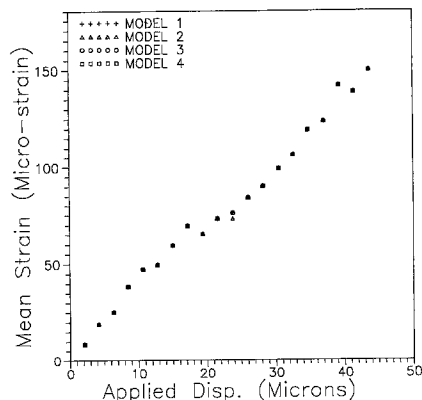
Grid-method Accuracy

Rigid-body Motion

The influence which rigid-body motion has on the accuracy of the strain calculations and the importance of camera-calibration choice is explored by subjecting a 5 × 5 (1 dot/mm) grid consisting of spots with 'step' (top-hat) intensity profiles to in-plane and out-of-plane translation, and in-plane rotation. Four types of camera calibration models are used:

Model (1)—No camera calibration

Model (2)—Image stretching and perspective correction $[a_4 = a_5 = a_6 = a_7 = a_{11} = a_{12} = a_{13} = a_{14} = 0$ in eq (4)]

Model (3)—Image stretching, perspective, and one-term distortion correction $[a_6 = a_7 = a_{13} = a_{14} = 0$ in eq (4)]

Model (4)—Image stretching, perspective, and two-term distortion correction

The actual rigid-body motion of the grid is monitored with a Hewlett Packard 5512 Laser Measurement System and the strain is calculated by the algorithms described in 'Automated Grid Method' above. The laser system is a heterodyned Michelson interferometer with a .04-micron accuracy. The grid spots used in these tests are characterized by approximate radii and grey-level differences of 15 pixels and 80 grey levels respectively. Fourteen image averages are used in these and subsequent tests.

The strain developed in the rigid-body-motion specimens should be zero, so the strain calculated for each calibration model represents a base-line error. Figures 1 and 2 show the mean x-strain component (parallel to the rows in the CCD camera) as a function of in-plane and out-of-plane motion for all four camera-calibration models respectively. The mean strain is found by calculating the strain at each grid-point location, and then finding the average. These curves show that the base-line strain error for all camera models is roughly the same, and that the sensitivity to in-plane and out-of-plane motion is −1.0 and 3.33 microstrain/micron respectively for this lens system and experimental arrangement. The sensitivity to out-of-plane motion results from an apparent change in focal magnification and, as expected, influences the normal strains to a much larger degree than the shear strain. The driving mechanisms behind the strain sensitivity to in-plane motion are not clear, but they may result from
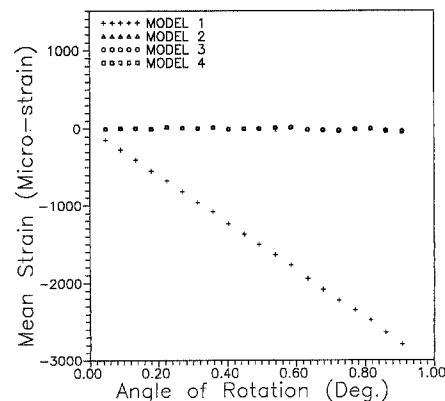

Fig. 2—X-strain error induced by out-of-plane rigid-body translation with the four-camera calibration models

Fig. 3—X-strain error induced by in-plane rigid-body rotation with the four-camera calibration models

nonuniform or time-dependent CCD response.[9] One redeeming feature of Figs. 1 and 2 is that the errors are competing and thus overall system error can be reduced under three-dimensional translation fields. The other normal and the shear strain sensitivities to rigid-body translation are roughly the same as that in Fig. 1.

While Figs. 1 and 2 show that each camera-calibration model has a similar response to rigid-body translation, Fig. 3 shows that the same is not true for in-plane rigid-body rotation. This figure shows that the shear-strain calculations for Model (1) (no calibration) is extremely sensitive to rigid-body rotation (3000 microstrain/degree). The other models have an approximate sensitivity of 30 microstrain/degree. Although not shown, the normal strain sensitivities for all the models are on the order of 100 microstrain/degree. The large shear strain found with Model (1) results from the affine transformation produced by the image stretching, therefore it only appears when the CCD camera and the frame grabber are not synchronized.

Uniaxial Tension

The accuracy of strain measurement with the automated grid method is evaluated by now placing the 5 × 5 (1 dot/mm) grid on an aluminum uniaxial tension specimen. The experimental arrangement used during these tests required a different aperture stop and focal magnification than those used in the rigid-body-motion tests described in the previous section. The strain in the specimen is monitored with both a resistance strain gage and the automated grid method. Strain increments of 50 microstrain are applied until a level of 1000 microstrain is reached. The strain at each grid point is calculated and the average is used for comparison with the resistance gage. The mean of the grid-spot strains is plotted in Fig. 4 as a function of the resistance gage strain. This figure shows that the average strains calculated with all four camera-calibration models are virtually identical. They are all consistently approximately 20-percent higher than the normal strain provided by the resistance gage, while the shear strains provided by all the camera models are very close to the expected zero level. This behavior suggests that some out-of-plane rigid-body motion is taking place during loading since this type of rigid-body motion affects the normal strains in the same way (adds to both or subtracts from both) and does not affect the shear strain. The standard deviation of the x-strain calculations for the four camera-calibration models is plotted in Fig. 5 as a function of the applied strain. It is apparent from this graph that models which include distortion correction induce a factor of two roughly greater uncertainty in the strain calculation. The average standard deviation of the grid strains which are calculated without using distortion correction is on the order of 40 microstrain; the accuracy is therefore estimated as plus/minus 120 microstrain (assuming a normal distribution). This estimate is made in light of the fact that Fig. 5 shows strain accuracy to be a function of the nominal strain in the specimen.

The uniaxial tension experiments indicate that the camera-calibration models which used distortion correction [Model (3) and Model (4)] produce roughly twice as much error in the strain calculation than those models which do not correct for distortion [Model (1) and Model (2)]. On the other hand, the rigid-body rotation experiments indicate that Model (1) (no calibration) produces excessive shear strain sensitivity. As a result, Model (2) is chosen as the most appropriate for the equipment used in

this study, and will therefore be used in the remaining sections of this paper.

Grid-spot Characteristics

The mathematical simulations performed in Ref. 9 show that the grid-spot grey-level profile, radius, grey-level difference, system noise, CCD pixel aspect ratio, nonuniform CCD response, and frame-grabber resampling all govern the limits of centroid-based grid methods. Grey-level profile and grid-spot diameter are the main focus of this section since the simulations in Ref. 9 show that grid spots with Gaussian intensity distributions provide an order of magnitude more accurate results when compared to grid spots with step-intensity distributions. Further, the spatial resolution of grid methods is governed by the number of grid spots placed on the specimen. CCD cameras have fixed pixel dimensions (typically on the order of 512 × 512), so there exists a limit to the number of spots which can fill the camera field of view and remain spatially unresolved. It is therefore important to use the smallest possible spot diameter which does not jeopardize the accuracy of the measurement technique.
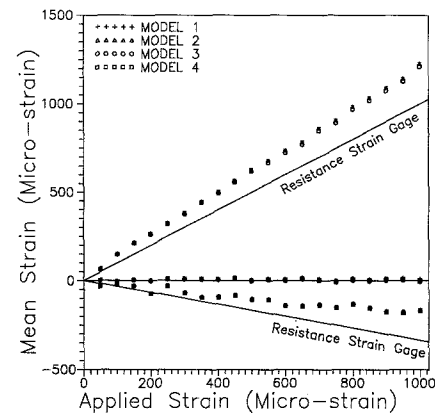

Fig. 4—Mean strain field in a uniaxial tension specimen found with the four-camera calibration models
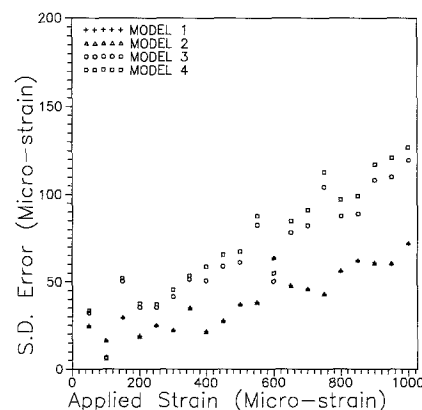

Fig. 5—Standard deviation of the X-strain component in Fig. 4 found with the four-camera calibration models
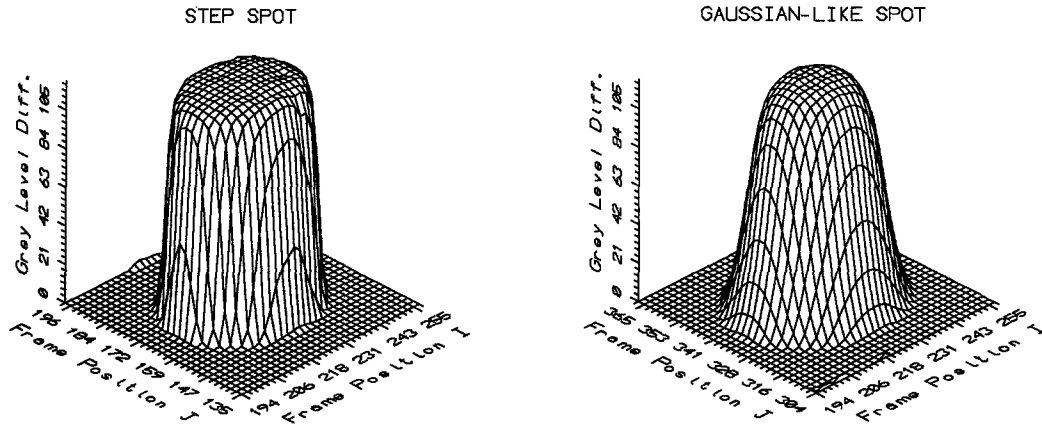
STEP SPOT

GAUSSIAN-LIKE SPOT

Fig. 6—Grey-level distributions for the step and Gaussian-like spots

Displacement error as a function of spot radius for Gaussian-like and step spots is explored by applying accurately controlled displacements simultaneously to equal diameter step and Gaussian-like spots. The spot diameters are controlled by changing the focal magnification of the CCD camera. A Gaussian-like intensity profile is defined as one which retains some of the smooth intensity transitions which are present in true Gaussian profiles. The Gaussian-like spots used in this test are produced by imaging the theoretically Gaussian intensity-output distribution of a single-mode optical fiber directly onto the replicating photographic emulsion. The non-linear response of photographic emulsion transforms the intensity distribution making the production of the truly Gaussian profiles studied in Ref. 9 virtually impossible. The emulsion transforms the relatively low frequency content in a true Gaussian spot to a spot whose frequency content exceeds the bandwidth of the CCD camera's transfer function.[8] Alternate replication techniques may be able to produce better quality Gaussian spots. Figure 6 shows the intensity distribution of both spots used in this test. The actual displacement of the grid spots is monitored with both the Hewlett Packard 5512 laser measurement system and the automated grid method. Spots of each diameter are given 30 displacement increments of .005 pixels each. The RMS error is calculated and plotted in Fig. 7 versus radius for both the Gaussian-like and step spots. However, these results do not indicate that the Gaussian-like spots consistently provide better results as suggested in Ref. 9. These data do show that the best possible displacement accuracy (assuming a normal distribution) for the step spot is .015 pixels, and that for the Gaussian-like spot is .006 pixels. The step-spot accuracy is very close to the .017-pixel accuracy predicted in Ref. 9. Figure 7 shows that both types of spots develop higher error when the spot radius becomes less than five pixels. If one takes this as the minimum acceptable radius, then a 50 × 50 grid is the highest allowable spot density (assuming a 512 × 512 CCD camera) without having resort to the combination of icons and camera translation.[1,7]

Reference 12 describes an attempt to decrease the signal-to-noise ratio by increasing the grey-level difference of the grid spots. The grey-level difference was increased from 70 to 120 by using white grid spots on a black background. This reduced the background blooming, thereby increasing the grey-level difference. However the blooming local to the white spots resulted in a spatially distorted grey-level profile which actually doubled the error in the strain calculations.

Perforated Strip

This final experiment uses the automated grid method to analyze the total displacements and strains developed in an aluminum perforated uniaxial tension specimen which is loaded so that plastic deformation occurs in the vicinity of the perforation. Figure 8 provides the requisite geometric details of the specimen and its loading. Symmetry of the specimen geometry and loading conditions enables a 3.3 dot/mm step-spot grid to be replicated onto a single quadrant of the specimen as depicted in Fig. 8. The specimen is loaded such that the far-field ϵ_{xx} is 2800 microstrain as monitored by a resistance strain gage. Similar specimens are monitored with 39.4-ℓpmm geometric moiré so as to provide a comparison to the grid-displacement measurements. Figures 9(a) and 9(b) show the comparison between the U and V fields found from
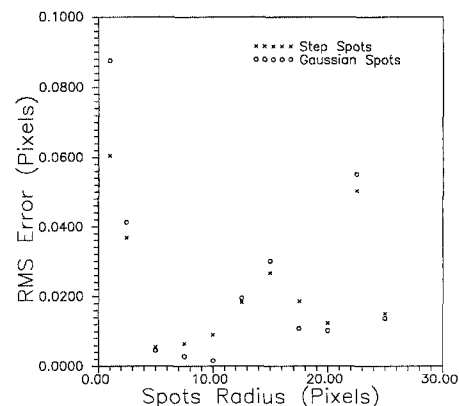

Fig. 7—In-plane translation error as a function of spot radius for the step and Gaussian-like spots

the grid and moiré methods. The upper contour plot provides the automated grid results, and the bold lines in these contour plots represent lines of constant displacement chosen to correspond the 39.4-ℓpmm moiré displacement interval shown in the adjacent fringe patterns. Also provided in Fig. 9 is a scaled representation of the grid spacing used in these experiments. When comparing the grid and moiré results it is important to recognize that the grid U and V fields were simultaneously measured from a single specimen, while the moiré U and V fields were measured from two different specimens. The small differences in the behavior between moiré and grid displacement fields can be attributed to slight different load levels.

The dashed lines in Fig. 9 are added to illustrate the ease in obtaining higher spatial resolution data with the automated grid method. The relatively high spatial resolution is obtainable from relative coarse (3.3 dot/mm) grid since biquadratic interpolation is an inherent feature of the automated grid method. The dashed contour lines represent a 5.08-micron interval in lines of constant dis-

placement. This contour interval was chosen arbitrarily. There are obvious limitations to the amount of interpolation that can be performed without jeopardizing data integrity. Figures 10 show the strain fields, in units of microstrain, which correspond to the automated grid-
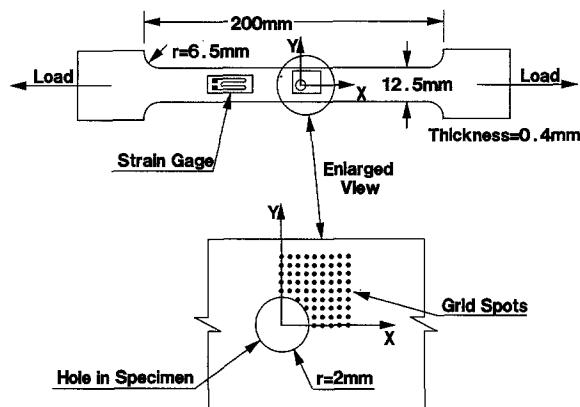

Fig. 10(a)—Experimental ϵ_{xx} distribution for the perforated strip

Fig. 8—Perforated strip with a grid placed on one symmetric quadrant subjected to uniaxial tension

Fig. 10(b)—Experimental ϵ_{yy} distribution for the perforated strip

(a)   (b)
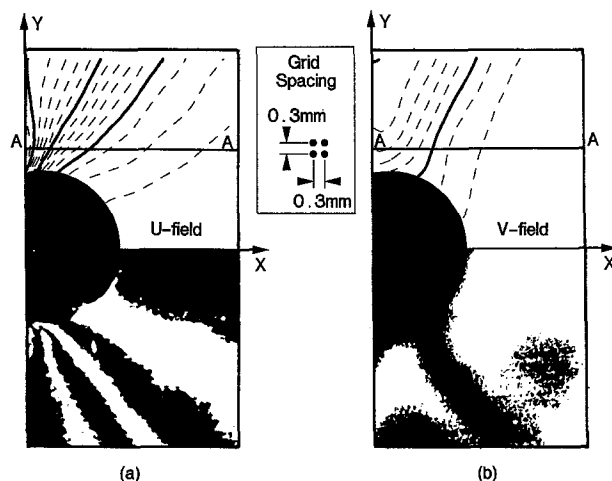
Fig. 9—(a) Automated grid and moiré U-displacement field. (b) Automated grid and moiré V-displacement field

Fig. 10(c)—Experimental ϵ_{xy} distribution for the perforated strip
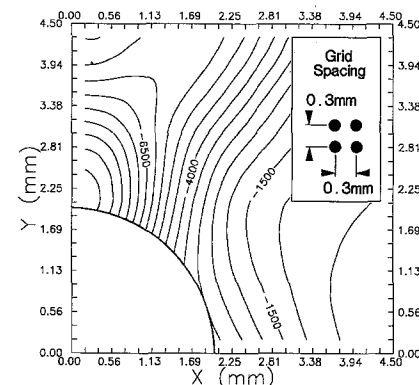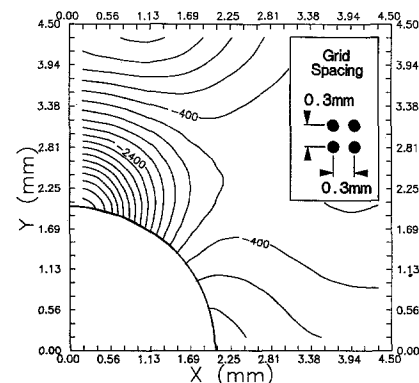
method-displacement measurements shown in Fig. 9. While an analytical solution does not exist for the perforated strip loaded to the plastic range, these strain fields exhibit good qualitative correlation with the strain fields which are expected from the geometric moiré (and grid) displacement fields. A more quantitative comparison of the strains found by the automated grid method is provided along the line $y = 2.54$ mm (line A-A in Fig. 9) and the strain found by geometric moiré along $y = -2.54$ mm (mirror image of line A-A but not shown in Fig. 9) is provided in Fig. 11. The solid lines labeled Exx, Eyy, and Exy in this figure represent the strain distributions found with the automated grid method, while isolated symbols represent the geometric moiré results. The agreement is best for the ϵ_{xx} strain distribution, with the ϵ_{yy} and ϵ_{xy} distributions showing only general agreement. The difference between automated grid and geometric moiré strain distributions is caused in part by the slight differences in specimen loading, but it is mainly caused by the limited number of fringes from which the moiré strain measurements can be made.

Conclusions

The important features which distinguish the automated grid method described in this paper are simplicity and speed. The simplicity of the algorithm enables full-field strain analysis to be accomplished in under 120 seconds with an 80286 PC compatible computer. Rigid-body motion and uniaxial tension tests are used for experimental characterization of the displacement and strain measurement limits of the centroid-based automated grid method, with particular emphasis on camera-calibration models.

The rigid-body motion and uniaxial tension tests reveal that lens-distortion correction actually increases the error in strain-field calculations which is in contrast to the result reported by Chao et al.[10] However, Chao et al.'s[10] stereo digital correlation used large camera angles with respect to their specimen, whereas in the present work the camera is almost normal to the specimen plane. Also, the influence of distortion correction is specific to the system hardware.

The rigid-body rotation tests demonstrate that perspective and image stretching must be included in the calibration model to avoid excessive sensitivity of shear strain to in-plane rigid-body rotation. This result applies only to

digital-image-processing systems in which the video camera and frame grabber are not synchronized, which is generally the case. The normal strain sensitivities to in-plane and out-of-plane rigid-body translation were measured to be -1.0 microstrain/micron and 3.33 microstrain/micron respectively. The analytically differentiated bi-quadratic surface technique for finding the in-plane strain tensor exhibited 20-percent systematic bias, and estimated strain error levels around 120 μ. The systematic bias is caused by out-of-plane rigid-body translation.

The rigid-body-motion tests comparing Gaussian-like and step spots did not reveal definitive proof that the Gaussian-like spots always provide better accuracy. Assuming a normal error distribution, displacement errors can be as low as .006 pixels with more common error levels around .02 pixels. The displacement error tests confirm some of the simulation results presented in Ref. 9; one of which is that grid spots less than five pixels in radius yield unacceptable error.

Finally, the automated grid method using step spots and a camera-calibration model which includes perspective and stretching transformations is used to investigate the displacement and strain fields surrounding a hole in an aluminum perforated strip subjected to uniaxial tension. The results compare favorably to those provided by geometric moiré.

Acknowledgments

The authors would like to thank Prof. M.A. Sutton of the University of South Carolina for his fruitful suggestions and constant encouragement, and the reviewers for their helpful comments.

References

1. Sevenhuijsen, P.J., "Photonics for Deformations," Proc. 5th Int. Con Mech., Montreal (1984).

2. Sevenhuijsen, P.J., "An Idea for a Simple Laser Grid Method for Measurement of In-plane Deformations," NRL-TR 74072L, Netherlands (April 1974).

3. Cardenas-Garcia, J.F. and Wu, M., "Further Development of Video Optical Diffractometry for Strain Measurement," Proc. 1989 SEM Spring Conf. on Exp. Mech., 73-79 (1989).

4. Berger, J.R. and Kriz, R.D., "An Improved Optical Diffraction Strain Measurement System," Proc. 1989 SEM Spring Conf. on Exp. Mech., 572-578 (1989).

5. Burger, C.P., Chona, R., Bowman, D.W., Lieder, R.M. and Parakh, Z.K., "High Temperature Failure of Materials," Proc. 1990 SEM Spring Conf. on Exp. Mech., 523-528 (1990).

6. Dennison, E.W. and Stanton, R.H., "Ultra-Precise Star Tracking Using Charged Coupled Devices (CCDs)," Proc. of SPIE (252), 54-63 (1980).

7. Fail, R.W. and Taylor, C.E., "An Application of Pattern Mapping to Plane Motion," EXPERIMENTAL MECHANICS, 30 (4), 404-410 (1990).

8. Sirkis, J.S. and Taylor, C.E., "Displacement Pattern Matching an Element Methods for Elastic-Plastic Stress Analysis," EXPERIMENTAL MECHANICS, 30 (1), 26-33 (1990).

9. Sirkis, J.S., "System Response to Automated Grid Methods," Opt. Eng., 29 (2), 1485-1493 (1990).

10. Choa, Y.J., Sutton, M.A., Peters, W.H. and Luo, P.F., "Measurement of Three-Dimensional Displacements and Deformations in Deformable Bodies Image Processing," Proc. 1989 SEM Spring Conf. on Exp. Mech., 139-146 (1989).

11. Sevenhuisjen, P.J., "Two Simple Methods for Deformation Demonstration and Measurement," Strain, 17 (1), (1981).

12. Sirkis, J.S. and Lim, T.J., "Accuracy Limits for Automated Grid Methods," Proc. 1990 SEM Spring Conf. on Exp. Mech., 498-505 (1990).

13. Tsai, R.Y., "An Efficient and Accurate Camera Calibration Technique for 3D Machine Vision," Comp. Vis. and Pat. Rec., 364-374 (May 1986).

14. Gonzales, R.C. and Wintz, P., Digital Image Processing, Addison Wesley (1987).

15. Lancaster, P. and Salkauskas, K., Curve and Surface Fitting: Introduction, Academic Press, London (1986).
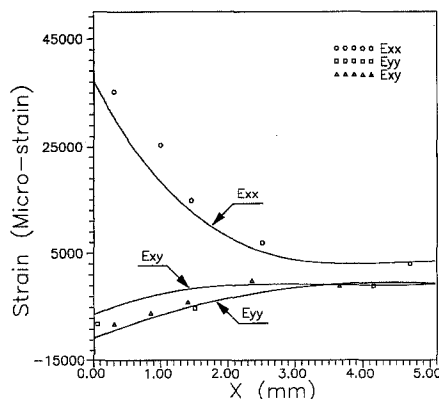
Fig. 11—Automated grid method and geometric moiré strain distributions along $y = 2.54$ mm and $y = -2.54$ mm respectively